5

The 'ultimate' cluster radio relic spectrum: observations from 150 MHz to 30 GHz

Radio relics are thin patches of diffuse synchrotron radio emission thought to form when intra-cluster medium particles are accelerated by cluster merger induced Mpc shock waves, through the diffusive shock acceleration mechanism. In this paper, we present observations from 150 MHz to 30 GHz of the 'Sausage' and 'Toothbrush' relics from the Giant Metrewave and Westerbork telescopes, the Karl G. Jansky Very Large Array, the Effelsberg telescope, the Arcminute Microkelvin Imager and Combined Array for Research in Millimeter-wave Astronomy. We securely detect both relics at 30 GHz, a factor of 2 higher than the the previous highest frequency measurement at 16 GHz. The integrated radio spectra of both sources clearly steepen above 2 GHz, at the $> 7\sigma$ significance level, confirming the spectral steepening of the integrated relic spectrum found by Stroe et al. (2014) for the 'Sausage' cluster and Trasatti et al. (2015) for Abell 2256. Our results strongly challenge the currently adopted formation mechanism of radio relics and suggest more complicated models have to be considered.

5.1   Introduction

Radio relics are polarized areas of radio emission extending located exclusively at the out-skirts of massive, post-core passage merging galaxy clusters (Feretti et al. 2012; Brunetti & Jones 2014). Relics are diffuse, low-brightness sources with arc-like morphologies extending over > 1 Mpc scales, preferentially oriented along the merger axis of their host cluster (Feretti et al. 2012). Observations at radio frequencies mainly below 5 GHz indicate that radio relics have steep integrated radio spectra well described by a single power law with $\alpha < -1$, where radio spectral index α is described as the flux F as function of the frequency ν: $F \sim \nu^{\alpha}$ (Feretti et al. 2012). Studies also found evidence for gradients of spectral index and curvature across radio relics (Orrú et al. 2007; van Weeren et al. 2010; van Weeren et al. 2012; Bonafede et al. 2012; Stroe et al. 2013). The synchrotron nature of these sources, coupled with the strong po-larization, indicates a significant anisotropy in the magnetic field structure. The observational results regarding the morphology, spectrum and polarisation of radio relics led to the inter-pretation that they are produced by synchrotron-emitting cosmic ray electrons accelerated by merger shocks through the diffusive shock acceleration mechanism (DSA; Ensslin et al. 1998). Weak travelling shocks with $M < 5$ can be produced when a small percentage of the energy released during massive mergers is dissipated in the form of wave fronts (Pfrommer et al. 2006).

However, more recently, evidence in tension with the simple, test-particle DSA picture has been found. From a theoretical point of view, low-Mach number shocks are not effi-cient enough to inject thermal particles to explain the amount of radio emission (Kang et al. 2007). Clearly detected X-ray shocks were found to have no or an offset radio counterpart (e.g. Russell et al. 2011; Ogrean et al. 2013, 2014), while in cases with a joint shock de-tection, a mismatch between the X-ray and the radio Mach number measurement was found (van Weeren et al. 2012; Ogrean et al. 2013). However, the discrepancy between the two Mach number estimation has been since partially alleviated, being possibly explained mainly by resolution effects affecting the radio measurement (Stroe et al. 2014). Very recently, high frequency radio measurements of relics have been published for the first time at 16 GHz with the Arcminute Microkerlvin Imager (AMI, Stroe et al. 2014) and the Effelsberg telescope at 10 GHz (Trasatti et al. 2015). Both studies find evidence for steepening of the radio spectrum at frequencies higher than 2 GHz. Erler et al. (2015) propose that the Sunyeav-Zeldovich effect (SZE; Sunyaev & Zeldovich 1972), the upscattering of cosmic microwave background photons by the intra-cluster medium electrons, could explain the steepening of the spectrum. However, Stroe et al. (2014) propose intrinsic relic physics causes for the steepening. The injection spectrum could not have a power law distribution or the magnetic field could be ordered and boosted at the shock location but turbulent in the downstream area. Addition-ally, at radio frequencies beyond 1 GHz we might be observing a range where test-particle DSA is not applicable (also supported by simulations by Kang 2015). Kang & Ryu (2015) obtain, through time-dependent DSA simulations of a spherical shock impinging on a magne-tised cloud of pre-accelerated relativistic electrons, relic spectra which gradually steepen from $(0.1 - 10)$ GHz range. However, the gradual steepening is not strong enough to fully explain the observations from Stroe et al. (2014).

The study of Trasatti et al. (2015) have integrated flux measurements of the Abell 2256 relic at only two frequencies beyond 2.5 GHz, at 5 and 10 GHz, while Stroe et al. (2014) have

one measurement, however at a much larger lever arm (16 GHz), meaning the actual shape of the high-frequency spectrum cannot be fully constrained. Theoretical models cannot be properly tested given the lack of evenly-spaced measurements above 2.5 GHz.

The clusters CIZA J2242.8+5301 ('Sausage'; Kocevski et al. 2007; van Weeren et al. 2010) and 1RXS J0603.3+4214 (van Weeren et al. 2012, 'Toothbrush') are ideal targets to alleviate the lack of high frequency data and study formation models for radio relics. Both clusters host a bright relic ($F > 0.15$ Jy at 1.4 GHz) towards their northern periphery, which extends over more than 1.5 Mpc in length, but less than 200 kpc in width. The 'Sausage' and the 'Toothbrush' importantly benefit form rich data below 2.5 GHz, which enabled van Weeren et al. (2012), (Stroe et al. 2013) and (Stroe et al. 2014) to find gradients of increasing spectral index, spectral curvature and electron age from the northern towards the southern edge of the relics.

We have performed new high-frequency observations of the two relics with the Karl G. Jansky Very Large Array (VLA) at 2.25, 2.75, 3.25 and 3.75 GHz, with the Effelsberg telescope at 5 and 10 GHz, with AMI at 16 GHz and with the Combined Array for Research in Millimeter-wave Astronomy (CARMA) at 30 GHz. We combine the new observations with the radio data already available from the Giant Metrewave Radio Telescope (GMRT), the Westerbork Synthesis Radio Telescope (WSRT) and AMI (van Weeren et al. 2012; Stroe et al. 2013, 2014) to produce a spectrum for the main radio relics well sampling a frequency range spanning 2.3 dex.

At the redshift of the two clusters, $z \sim 0.2$, 1 arcmin corresponds to a scale of 0.2 Mpc. All images are in the J2000 coordinate system.

5.2 Observations & data reduction

For our analysis we combine already exiting observations with new data for the 'Sausage' and 'Toothbrush' relics. The frequencies of the observations can be found in Table 5.1. Standard calibration was applied to all the data sets, including flagging, bandpass and gain calibration. The details of the reduction of the existing GMRT and WSRT datasets can be found in van Weeren et al. (2012) and (Stroe et al. 2013).

5.2.1 VLA data

Observations of the 'Sausage' cluster in S band were performed in D array configuration with the VLA on 27 January 2013. Data was recorded in full polarisation, in 16 spectral windows of 128 MHz each, spanning a bandwidth of 1 GHz between 2 and 3 GHz. Each spectral window was further subdivided into 64 channels. The 1.5 h on source-time were equally divided over three separate pointings to cover the cluster region. Two primary calibrators were observed, 3C138 and 3C147. J2202+4216 was used as a secondary calibrator. The pointing centres for the cluster were: RA=22:43:19, DEC=+53:05:28; RA=22:42:36, DEC=+53.07:29 and RA=22:42:41, DEC=+52:58:09. The data were calibrated calibrated with the Common Astronomy Software Applications package[1] (CASA version 4.3 McMullin et al. 2007). The data were first corrected for the antenna offset positions and elevation dependent gain curves. The

---

[1]http://casa.nrao.edu/

Table 5.1: Summary of the frequencies at which observations have been made for the 'Sausage' and 'Toothbrush' radio relics. In both cases, the observations span from 150 MHz to 30 GHz.

Source	Telescope	Frequencies
	GMRT	150, 325, 610 MHz
	WSRT	1230, 1380, 1710, 2270 MHz
'Sausage'	VLA	2250, 2750, 3250, 3750 GHz
15 frequencies	Effelsberg	4.85, 8.35 GHz
	AMI	15.85 GHz
	CARMA	30 GHz
	GMRT	150, 240, 324, 608 MHz
	WSRT	1230, 1380, 1710, 2270 MHz
'Toothbrush'	Effelsberg	4.85, 8.35 GHz
12 frequencies	AMI	15.85 GHz
	CARMA	30 GHz

data were also Hanning smoothed and strong radio frequency interference (RFI) was removed with the 'tfcrop' option of the task flagdata(). The flux-scale for the primary calibrators was set using the calibrator model image provides by casapy and taking the (Perley & Butler 2013) scale. We then determined an initial bandpass correction using the primary calibrator sources. This is done to remove the strong bandpass rolloff at the edges of the spectral windows which hinders the detection of RFI. RFI was then removed with the with AOFlagger (Offringa et al. 2010). After RFI removal, we determined initial gain corrections using the central 10 channels of the spectral windows. These corrections were pre-applied before finding the delay solutions and subsequent final bandpass solutions. By pre-applying the gain solutions we remove any temporal variations in the gains which would otherwise effect the bandpass and delay terms. The gain solutions were then re-determined for all calibrator sources but now pre-applying the bandpass and delay solutions. Next we bootstrapped the primary flux-scale to the secondary calibrator. The final calibration solutions were applied to the target fields.

For imaging purposes (see §5.3.1) observations was split into four datasets, each with a bandwidth of 0.5 GHz, with central frequencies 2.25, 2.75, 3.25 and 3.75 GHz.

5.2.2   Effelsberg data

The observations were performed with the Effelsberg 100-m Radio Telescope in October/November 2010, January 2011, October 2011 and August 2014 using the 3.6 cm (8.35 GHz with 0.4 GHz bandwidth) single-horn and λ6.3 cm (4.85 GHz with 0.5 GHz bandwidth) dual-horn receiving systems installed at the secondary focus. The radio sources 3C 48, 3C 138, 3C 147, 3C 286 and 3C 295 were observed as flux density and pointing calibrators, using the flux densities from Peng et al. (2000). At 8.35 GHz we obtained 46 maps for 'Sausage' (in Stokes I, Q and U) and 40 in Stokes I and 20 in Stokes Q and U for 'Toothbrush' scanned alternatively in RA and DEC directions. At 4.85 GHz we obtained 32 maps for 'Sausage' and 12 for 'Toothbrush' (in Stokes I, Q and U) scanned in azimuthal direction. The main part of data reduction, introducing initial examination of the data and the flagging of bad visibilities, was accomplished

using the NOD2-based software package (Haslam 1974). Thereby, each map in I, Q and U was checked for scanning effects, RFI and incorrect baselevels. The dual-horn maps at 4.85 GHz were combined using software beam-switching and transformed into the RA, DEC coordinate system. All maps in Stokes parameters I, Q and U were averaged and combined using the basket-weaving method (Emerson & Graeve 1988). The final maps were smoothed to 90 arcsec at 8.45 GHz and 159 arcsec at 4.85 GHz.

5.2.3 AMI data

Observations for the 'Toothbrush' relic were taken at ~ 16 GHz with the AMI (AMI Consortium: Zwart et al. 2008) Small Array (AMI-SA), in a single pointing on 8 June 2012 achieving ~ 2*arcmin* resolution. The relics was subsequently observed with the Large Array (AMI-LA) in a 4-point mosaic on 7 November 2013, achieving a resolution of ~ 30 arcsec. As explained in Stroe et al. (2014), the two arrays provide complementary resolution and uv coverage, the AMI-SA mainly detecting very large scale emission (> 10 armin) and AMI-SA being more suited for more compact objects. We follow the same reduction steps described in Stroe et al. (2014) for the 'Sausage' cluster.

5.2.4 CARMA data

The 'Sausage' and 'Toothbrush' relics were also observed with higher resolution (15 element 6.1-m and 10.4-m dishes) of CARMA in rasters focused on the relic areas, on 22 or May and 10 July 2014, respectively. Typical calibration steps were applied in the CASA.

5.3 Imaging and flux measurements

The goal for our analysis is to study the integrated spectrum of the two radio relics. Therefore, the fluxes have to be measured in radio image which sample the same scales on the sky, at the same resolution. We image the datasets using the CLEAN algorithm, with uniform weighting of the uv points at the same pixel (1 arcsec per pixel) and image size and correct all of them for the effects of the primary beam attenuation.

5.3.1 Radio images

We produced interferometric images using the CLEAN algorithm and refined them through the process of self-calibration. In the case of the VLA data, we decided to group the data into four 0.5 GHz wide to allow flux measurements at central frequencies of 2.25, 2.75, 3.25, and 3.75 GHz with sufficient S/R and without being hindered too much by spectral variations within a 0.5 GHz band. For these four VLA image, the three pointings were jointly convolved and imaged, taking the primary beam into account, using the "mosaic" option of the clean() task in CASA.

For the self-calibration we started with two rounds of phase-only calibration and this was followed by two final rounds of amplitude and phase calibration. The amplitude solutions were normalized to 1.0 to prevent drifting of the flux-scale. For imaging during the self-

Table 5.2: Imaging parameters and data used in combination for producing integrated spectra. All the data was convolved to the image with the lowest resolution. At the higher resolution set, the AMI-LA has the lowest resolution. For the lower resolution set, the limitation was the Effelsberg 5 GHz map.

Source	Type	uv range kλ	Max scale '	Resolution "	Telescope	Frequencies GHz
'Sausage'	Low resolution	> 0.2	~ 17	147	GMRT, WSRT, Effelsberg, AMI-SA	0.15, 0.325, 0.61, 1.2, 1.4, 1.7, 2.3, 4.85, 10.45, 15.85
	High resolution	> 0.8	~ 4	40	GMRT, WSRT, VLA, AMI-LA, CARMA	0.15, 0.24, 0.325, 0.61, 1.2, 1.4, 1.7, 2.25, 2.3, 2.75, 3.25, 3.75, 15.85, 30
'Toothbrush'	Low resolution	> 0.2	~ 17	147	GMRT, WSRT, Effelsberg, AMI-SA	0.15, 0.24, 0.325, 0.61, 1.2, 1.4, 1.7, 2.3, 4.85, 10.45, 15.85
	High resolution	> 0.8	~ 4	40	GMRT, WSRT, AMI-LA, CARMA	0.15, 0.24, 0.325, 0.61, 1.2, 1.4, 1.7, 2.3, 15.85, 30

calibration we used Briggs weighing with a robust factor of 0.0 (Briggs 1995). To aid the deconvolution we used clean boxes.

We produce two sets of images using different uv ranges from our interferometric data, in order to study the diffuse emission at on different scales. All images were primary beam corrected. The details of the imaging parameters and the data used can be found in Table 5.2. To probe spatial scales of up to $\sim$ 4 arcmin, we use only data at uv distances beyond 0.8 kλ and convolve the images $\sim$ 0.5 arcmin resolution. For probing scales up to 17 $\sim$ arcmin, we data at uv distances beyond 0.8 kλ and convolve the images to 2.5 arcmin resolution. The low-resolution images also serve as potential counterparts for the Effelsberg single dish images, which measure total power. Note, however, that since radio relics are extremely diffuse objects, any spatial filtering applied by the interferometer will heavily affect the measured flux. For example, the 'Sausage' relic at 150 MHz flux drop by a factor of 2 when going using data beyond 0.2 kλ to using only data beyond 0.8 kλ. Therefore, Effelsberg measures a much higher flux than inferred from the interferometric observations only.

The low (from Effelsberg) and high (from AMI-LA and CARMA) resolution images, produced with uniform weighting and common uv-cut are shown in Figures 5.1 and 5.2 for the 'Sausage' and 'Toothbrush' relics, respectively. Note that even in uniform weighted images, which emphasise point sources and suppress diffuse emission, the relics are clearly detected till 30 GHz. In the low resolution images, the relics are detected at very high signal-to-noise ($S/N > 16$), but deblending the emission from the point sources is non-trivial.

5.3.2 Obtaining flux measurements

We measure the flux of the relics at the various frequencies using the same region for integration on uniform weighted maps, sampling the same scales on the sky and convolved to the lowest resolution available.

For all but the AMI data, we adopt a flux-scale uncertainty f of 10 per cent, following Stroe et al. (2013), resulting from from telescope pointing errors and imperfect calibration. The AMI flux scale is precise within 5 per cent according to AMI Consortium: Davies et al. (2011). The error ΔF on the integrated flux F is calculated as function of the flux scale error and image noise σ_{RMS}:

$$\Delta F = \sqrt{(fF)^2 + N_{\mathrm{beams}}\sigma_{\mathrm{RMS}}^2}, \qquad (5.1)$$

where N_{beams} is the number of beams spanned by the source.

As explained in Stroe et al. (2014), both AMI sub-arrays measure a single polarisation. However, lower frequency, high resolutions measurements show that the 'Sausage' and the 'Toothbrush' relic are polarised (van Weeren et al. 2010; van Weeren et al. 2012). Because the AMI reduction pipeline assumes the source is unpolarised, the flux of a polarised source needs to be reduced. Following the method from Stroe et al. (2014), the AMI integrated flux of the 'Sausage' relic has to be decreased by 24 per cent, compared to the single polarisation measured by AMI. IN the case of the 'Toothbrush', the polarisation values from (van Weeren et al. 2012) were used to derive a flux reduction of 12 per cent. Note however, that even if we assumed the sources to be fully unpolarised, their flux would not change the overall integrated spectrum fits significantly (see below and §5.4).

The 'Sausage' and 'Toothbrush' relic flux measurements at high and low resolution can be found in Table 5.3. Note that the low-resolution data are not fully comparable given interfer-

ometers resolve out flux detected by Effelsberg. Therefore the low-resolution measurements are give for reference only. In the ensuing analysis, we only use the high-resolution images, which are made from fully comparable data.

As found by Stroe et al. (2014), a single power law provides a poor description of the data. We therefore fit the spectrum of each relic with a broken power law using weighted least-squares regression, where each point is down-weighed according to its error (as per equation 5.1). We fit the flux for the entire source, as well as split the source in two regions (left and right half for the 'Sausage' relic and the subareas B1 and B2+B3, see Figure 5.2). The measurements and the results of the fit can be found in Figures 5.3 and 5.4, for the 'Sausage' and 'Toothbrush' relics respectively. We find that the low-frequency spectrum (< 3 GHz) greatly differs from the high frequency spectrum (2.5 GHz) for both sources. The low frequency spectrum for the 'Sausage' relic has a spectral index of $\alpha = -0.86 \pm 0.04$, while beyond 2.5 GHz this steepens to -1.91 ± 0.14 (difference significant at the 7.2σ level). In the case of the 'Toothbrush', the low frequency spectrum differs from the high frequency one at the 8.5σ level (-0.92 ± 0.04 versus -1.53 ± 0.06). Note that the results hold when splitting the source into two subareas.

5.3.3   Possible systematics decreasing high frequency fluxes

Under the assumption that the test particle DSA relic formation model is correct, we explore possible systematic effects which can cause the high frequency measurements to be biased low. The scenarios discussed are either instrumental in nature or to physics operating outside of the radio relics.

Flux scale and polarisation correction

An issue with the flux scale at a particular frequency could result in an underestimation of the flux. However, the integrated spectra of point sources in the GMRT, WSRT, VLA, AMI and CARMA data are described by power law, indicating all the observations are on the same flux scale. Also note the very good agreement between the WSRT and VLA measurements at ~ 2.3 GHz for the 'Sausage' relic. Moreover, it is highly unlikely that the flux scale is biased low for independent measurements with three telescopes of two sources.

As explained in §5.3.2, AMI assumes that sources are unpolarised and the fluxes measured for the relics need to be corrected, since they are polarised. As explained in Stroe et al. (2014), the polarisation fraction has to be assumed from lower-frequency measurements. Note however that the the polarisation correction leads to a reduction of the flux of max 30 per cent, which would leave the spectral index of the fits unchanged within the error bars. Additional support for the steepening, irrespective of the polarisation correction from AMI comes from CARMA. CARMA measures full polarisation, so no assumptions need to be made for the relics' integrated fluxes. The CARMA measurements fully corroborate the steepening observed by AMI at 16 GHz, in both the 'Sausage' and the 'Toothbrush' relics.

We therefore conclude that flux scale or polarisation correction issues cannot explain the steepening of the relic spectrum at high frequencies.
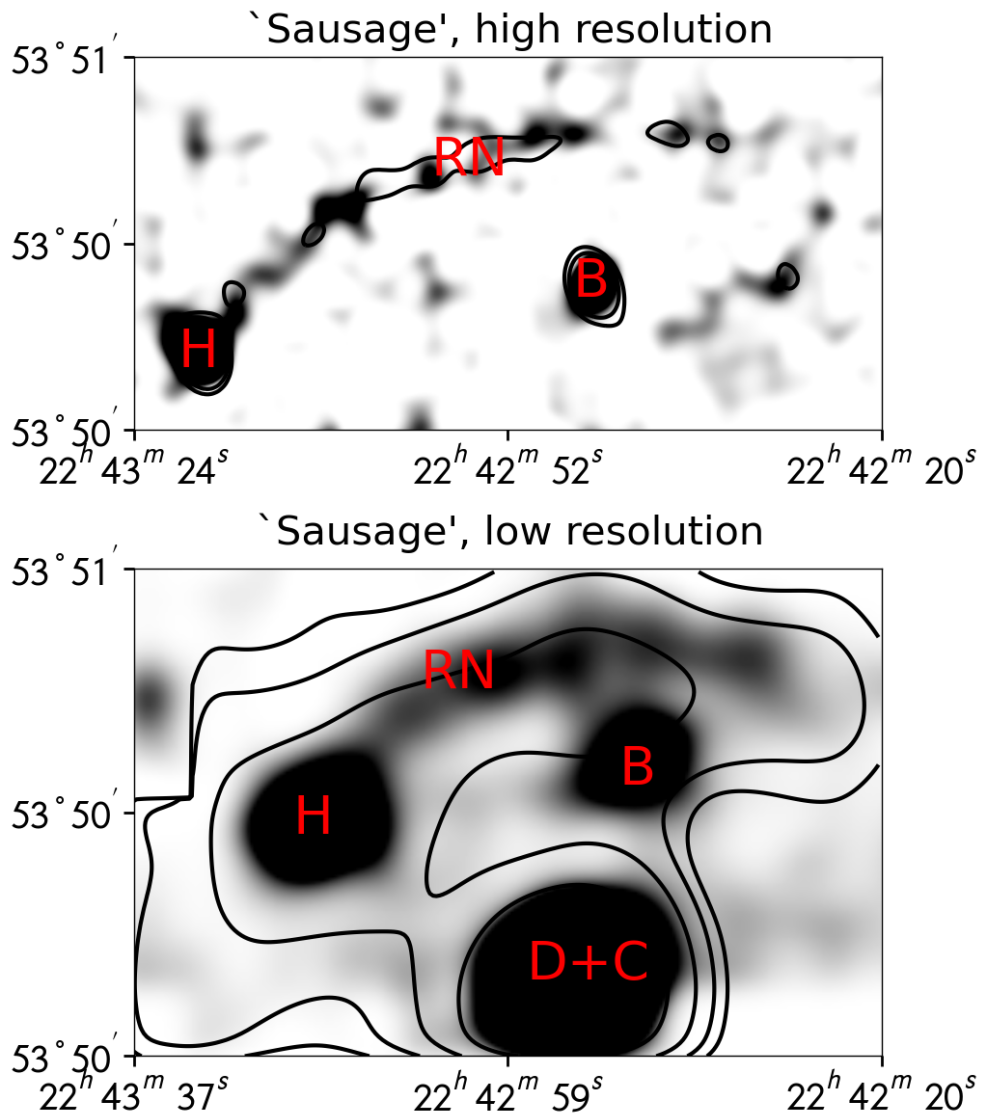
Figure 5.1: Uniform-weighted low and high resolution image of the 'Sausage' cluster. The top panel shows the CARMA image in grayscale and the AMI-LA image in contours draw at $[4, 8, 16, 32] \times \sigma_{RMS}$. The bottom panel shows the Effelsberg 10 GHz image in grayscale and the 5 GHz in contours at $[4, 8, 16, 32] \times \sigma_{RMS}$. We label the source as Stroe et al. (2013).
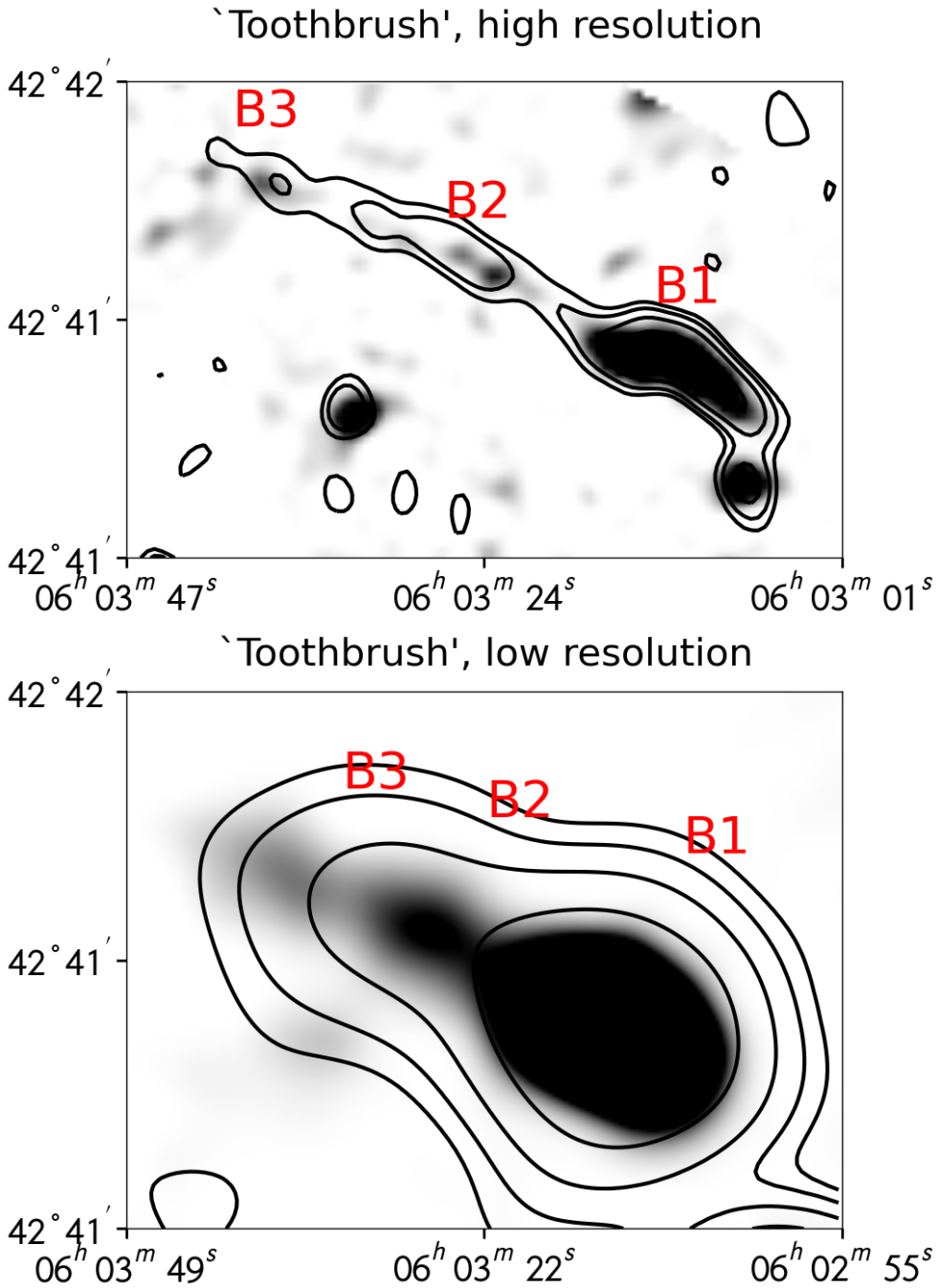
Figure 5.2: Same as Figure 5.1, but for the 'Toothbrush' relic. Sources are labelled according to van Weeren et al. (2012).

Contamination from point sources

Several radio galaxies are located nearby the relics, which especially in the low resolution images, might blend with the diffuse emission. This is especially true for the 'Sausage' relic, which has in neighboured by an unrelated radio AGN towards its eastern edge. However, radio galaxies are expected to have a flatter ($\alpha \sim -0.7$) integrated index compared to the radio relics, and will, if anything, bias high the flux measurement of the relics. In the higher resolution images, blending is not a significant contaminant, since no bright radio sources are located too close or embedded in the diffuse emission.

Sunyaev-Zeldovich decrement

At frequencies below $\sim$ 225 GHz, the SZE is detected in decrement causing a decrease in the measured fluxes. Even though that relics are located far away from the cluster centre, where the SZE is strongest, Erler et al. (2015) argue that shock compression could boost the signal, leading to up to 30 per cent decrease at 10 GHz for Effelsberg observations of the relic of Abell 2256 (Trasatti et al. 2015). However, the effect is expected to be negligible for AMI-LA and CARMA observations for a number of reasons. The resolution of AMI-LA and CARMA is a factor of > 2 higher than Effelsberg and the largest scale detectable is limited by virtue of interferometric observations (versus Effelsberg which is a single dish and measures total power). The other differences to the conditions of Abell 2256 is the distance of the relic from the cluster centre. (Trasatti et al. 2015) argue that the decrement is of the order of 30 per cent at the distance of the relic from the cluster center, which is about 500 kpc. At the distance of 750 kpc the SZE induced decrement drops to 15 per cent. However, the 'Sausage' and 'Toothbrush' relics are located about 1.5 Mpc away from the cluster centre, hence the SZE contamination would be very small (by extrapolation, at the level of < 5 per cent). Note that even if a significant decrement of a factor of 2 would be affecting the the AMI and CARMA data that would still not be enough the explain the discrepancy. By extrapolating the low frequency spectrum of the 'Toothbrush', the AMI and CARMA fluxes would have to be 3.5 and 6 times higher than measured, respectively. In the case of the 'Sausage' the fluxes predicted from the low frequency spectrum are more than 10 times higher that those measured.

5.4 Why is the integrated relic spectrum steepening?

Stroe et al. (2014) and Trasatti et al. (2015) found evidence for steepening of the high frequency (> 5 GHz) spectrum of radio relics which challenge the currently adopted view that relics are formed by shock acceleration at travelling shock fronts. In this paper, by using measurements at $\sim$ 15 independent frequencies we find that the high frequency spectrum of the 'Sausage' and 'Toothbrush' relics differ significantly (> 5σ). After disproving the possibility of systematics biasing the flux measurements, we now discuss possible physical scenarios which would lead to a curved integrated relic spectrum.

Spectral model fitting to spatially-resolved, low-frequency observations of 'Sausage' relic indicates an injection index of -0.77 (Stroe et al. 2014). The 'Toothbrush' low-frequency data indicate an injection index of about -0.6 (van Weeren et al. 2012), but given resolution effects operating on low-frequency radio data, the injection index is probably steeper (Stroe et al. 2014).

Table 5.3: Integrated radio spectrum of the 'Sausage' and 'Toothbrush' relics using two imaging modes. We mainly use the higher resolution mode which probes emission up to 4 arcmin on the sky. We also report the values for the low-resolution mode that probes emission up to 17 arcmin scales. Note however that, while the high resolution data are fully comparable, the low resolution data are not imaged in the same way. Hence, we report the values for the low resolution images for reference purposes only. For a list of caveats of the low resolution imaging, please see §5.3.2 and §5.3.3.

Freq (GHz)	0.15	0.24	0.325	0.61	1.2	1.4	1.7	2.25	2.3	2.75	3.25	3.75	4.85	8.45	16	30
'Sausage', low resolution																
Flux (mJy)	764.7		372.2	173.8	107.6	99.9	73.2		39.7				24.3	21.6	4.5	
Error (mJy)	89.7		44.7	18.3	11.1	10.3	7.6		5.1				2.7	4.3	1.0	
'Sausage', high resolution																
Flux (mJy)	655.3		286.9	197.3	125.7	117.3	91.2	58.1	48.3	50.0	36.1	16.5			0.8	0.6
Error (mJy)	67.8		29.6	19.8	12.6	11.8	9.2	5.9	5.0	5.1	3.7	2.1			0.2	0.3
'Toothbrush', low resolution																
Flux (mJy)	3900.5	1998.5	1020.6	803.4	386.7	320.0	252.9		181.6				79.3	82.0	8.9	
Error (mJy)	390.3	200.0	102.4	80.4	38.7	32.0	25.3		18.2				8.7	4.8	0.5	
'Toothbrush', high resolution																
Flux (mJy)	2637.7	1342.1	744.1	699.0	334.2	287.1	231.2		163.1						10.6	2.7
Error (mJy)	263.9	134.3	74.4	69.9	33.4	28.7	23.1		16.3						0.6	0.4
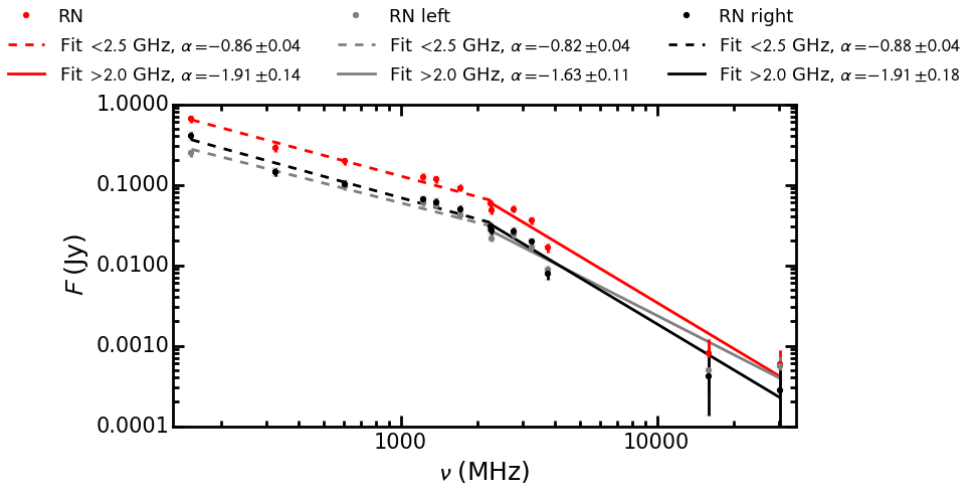
Figure 5.3: Integrated spectrum of the 'Sausage' radio relic measured at ∼ 30 arcsec resolution from 150 MHz to 30 GHz. There is clear evidence for spectral steeping beyond 2.5 GHz. A single power law does not fit the data, while a broken power law provides a much better description. Note the results hold even when we split the source in two halves.
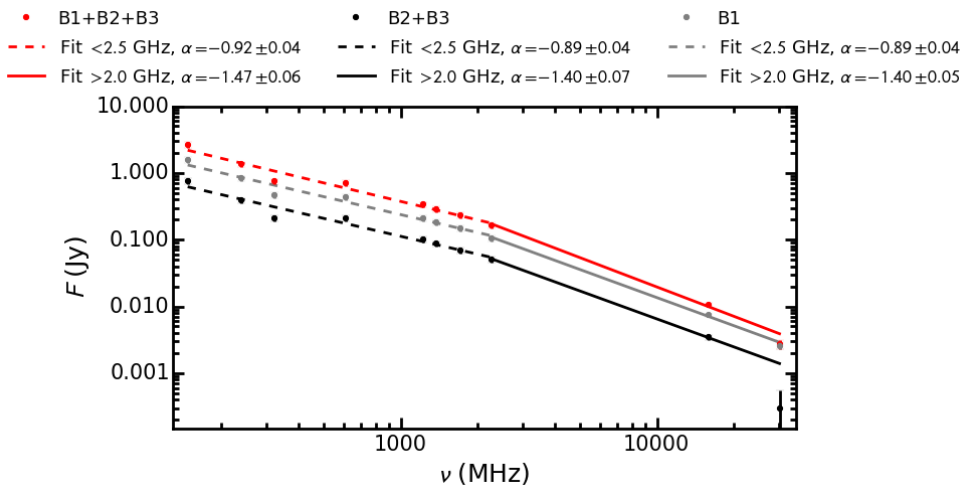
Figure 5.4: Same as Figure 5.3, but for the 'Toothbrush' relic.

In the simple, test-particle DSA scenario the shock strength is constant in time, the magnetic field is constant across the source and thermal particles are injected at the same rate. Under these assumptions, the index of the integrated spectrum should be 0.5 steeper than the injection index (Ensslin et al. 1998) and the injection index $\alpha_{\rm inj}$ can be directly translated to a Mach number through $M = \sqrt{(2\alpha_{\rm inj} + 3)/(2\alpha_{\rm inj} + 1)}$. This only holds if we are observing the spectrum away from the break frequency ($\nu_{\rm br}$), where we detect the electrons which have started to lose energy through synchrotron and inverse Compton processes. However, the low frequency spectral index of the two relics is about -0.9. If we assume we are observing far away from $\nu_{\rm br}$, this is inconsistent with the DSA theory, as subtracting 0.5 would result in an injection index that is too flat and an infinite Mach number.

Kang et al. (2012) perform DSA simulations tailored to the 'Sausage' relic and find a good agreement to the observed low-frequency (< 1.5 GHz) spectrum. However, the authors note that they models fails to reproduce the uniform brightness distribution across the source and the overall arc-like shape of the relic. Additionally, Kang (2011) and Kang & Ryu (2011) show that even when pre-accelerated particles are considered, the overall spectrum shape is conserved, while only the normalisation changes, because of the more efficient particle injection. Therefore, the DSA acceleration scenario, even when modified for relativistic particles, cannot explain the steepening of the spectrum towards high frequencies.

Furthermore, Vazza et al. (2015) show that the DSA (re)acceleration prediction for γ-rays is in stringent tension with upper limits placed by the Fermi Gamma-ray Space Telescope.

5.4.1 Adiabatic compression

Ensslin & Brüggen (2002) propose a relic formation scenario where a cocoon of fossil plasma deposited in the ICM by past radio galaxy activity could be revived through adiabatic compression by the passage of the shock. This model predicts a relic curved spectrum, as the one we see in the observations, but fails to reproduce a number of characteristics, as was previously pointed out by van Weeren et al. (2010), van Weeren et al. (2012) and Stroe et al. (2013). The low-frequency spectrum we observed is much flatter than expected from adiabatic compression. The Ensslin & Brüggen (2002) model also predicts a disruption of the cocoon into rich filamentary structure, which is not seen in either of our relics. Additionally, it would be highly unlikely to get radio lobes of more than 1.5 Mpc in length to explain the sizes of the 'Sausage' and 'Toothbrush' relics.

5.4.2 Structure in the Mach number or magnetic field distribution

A possibility of breaking the assumptions of test-particle DSA is if the magnetic field or Mach number are not uniform across the source causing anisotropies in the rate of particles are injected. The Mach number for example would mildly strengthen as it propagates outwards, impinging on lower density and lower temperature ICM gas (Brunetti & Jones 2014). However, observations of the brightness distribution, spectral index and electron age of the two relics indicate an extremely uniform structure, suggesting anisotropies in the Mach number are not a pivotal factor in shaping the relic spectrum (van Weeren et al. 2010; van Weeren et al. 2012; Stroe et al. 2013, 2014).

Simulations indicate that magnetic fields at the location of the shock are aligned and amplified (Iapichino & Brüggen 2012), while significant turbulence develops in the shock downstream area (Paul et al. 2011). A slowly decaying magnetic field from the shock region into the downstream area would lead to a decreasing cooling rate of the electron away from the shock. A magnetic field stronger at the shock than in the downstream area would lead to an integrated spectrum dominated by the freshly accelerated electrons located in the immediate vicinity of the shock front, therefore predicting a spectrum which is flatter than the DSA prediction. In order to reproduce a curving spectrum, we would need to amplify cooling in the downstream area. However, there is no plausible scenario of how this could happen.

Additionally, the turbulences in the downstream area might re-accelerate the particles injected by the shock, instead of suppressing the high frequency emission. Any downstream re-acceleration would be expected to boost the brightness of emission of aged electrons, most likely leading to a very flat spectrum, rather than a curved one. Additionally, turbulent re-acceleration is a slow process as it requires the large bulk motions to cascade into small scale turbulence (>> 100 Myr) which can actually inject particles (Brunetti & Lazarian 2007).

This scenario could further tested with high-resolution images at 4 GHz from VLA, which would better resolve the relic, pointing out possible anisotropies in the brightness distribution not visible at current resolutions (e.g. filaments) as well as variations in the magnetic field strength (van Weeren, in prep).

5.4.3   Seed population with energy distribution cut-off

(Kang & Ryu 2015) perform DSA simulations matched to the 'Sausage' relic, which indicate that a seed population with a break in the energy distribution, once re-accelerated by the shock would result in a steepening integrated spectrum. The authors suggest that electrons sourced from past AGN activity or previous shocks, have since aged, resulting in a distribution with an exponential fall-off a high energies. Fossil electrons previously accelerated by accretion shocks would reside at a few 100 MeV energies and have a very long lifetime of a few Gyr, without being directly detectable in the radio. However, none of the scenarios they tested fully matched observations from Stroe et al. (2014), and the authors conclude additional processes apart form radiative losses might be operating in radio relics.

5.5   Conclusions

In this paper, we have presented a number of high frequency (> 2.5 GHz) radio observations of the 'Sausage' and 'Toothbrush' relics. We combined these new measurements with GMRT and WSRT to study the relic spectrum over 2.5 dex in frequency.

- We successfully detect the 'Sausage' and 'Toothbrush' relics at high-radio frequencies up to 30 GHz.

- We find compelling evidence for steepening in the high frequency spectrum of both relics (at the $> 7\sigma$ significance level). The low frequency spectrum of both the 'Sausage' and 'Toothbrush' relics is well described by a single power law with spectral index ~ -0.9. The high spectrum is steeper that ~ -1.45 in both cases.

- The steepening cannot be explained by systematics such as flux scale errors, polarisation corrections, point source and SZE contamination.

- Simple test particle DSA cannot explain the observed spectrum. A possible explanation would be that the relics are formed through shock acceleration of seed relativistic electrons observed above the break frequency.

The models currently tested are all DSA-based with variations in the seed population. However, the mismatch between the models and the observations seems to suggest it is necessary we revisit the theory of radio relics. Therefore, the development of new theoretical models, building upon the observations presented here, is necessary. To attain this goal, high frequency data is crucial. Unfortunately, given the impending decommissioning of CARMA, the spectral width of the observations presented here is likely to be unsurpassed until upcoming very low and very high frequency instruments are fully rolled out with accurate flux scales, high resolution (e.g. Low Frequency Array, LOFAR, long baselines) and large field of view (e.g. low bands of Atacama Large Millimeter/submillimeter Array, ALMA).

Acknowledgements

Bibliography

AMI Consortium, Davies, M. L., Franzen, T. M. O., et al. 2011, MNRAS, 415, 2708

AMI Consortium, Zwart, J. T. L., Barker, R. W., Biddulph, P., et al. 2008, MNRAS, 391, 1545

Bonafede, A., Brüggen, M., van Weeren, R., et al. 2012, MNRAS, 426, 40

Briggs, D. S. 1995, PhD thesis, New Mexico Tech, USA

Brunetti, G., & Jones, T. W. 2014, International Journal of Modern Physics D, 23, 1430007

Brunetti, G., & Lazarian, A. 2007, MNRAS, 378, 245

Dressler, A. 1980, ApJ, 236, 351

Drury, L. O. 1983, Reports on Progress in Physics, 46, 973

Emerson, D. T., & Graeve, R. 1988, A&A, 190, 353

Ensslin, T. A., Biermann, P. L., Klein, U., & Kohle, S. 1998, A&A, 332, 395

Ensslin, T. A., & Brüggen, M. 2002, MNRAS, 331, 1011

Erler, J., Basu, K., Trasatti, M., Klein, U., & Bertoldi, F. 2015, MNRAS, 447, 2497

Feretti, L., Giovannini, G., Govoni, F., & Murgia, M. 2012, A&Ar, 20, 54

Haslam, C. G. T. 1974, A&A, 15, 333

Iapichino, L., & Brüggen, M. 2012, MNRAS, 423, 2781

Kang, H., Ryu, D., Cen, R., & Ostriker, J. P. 2007, ApJ, 669, 729

Kang, H. 2011, Journal of Korean Astronomical Society, 44, 49

Kang, H., & Ryu, D. 2011, ApJ, 734, 18

Kang, H., Ryu, D., & Jones, T. W. 2012, ApJ, 756, 97

Kang, H. 2015, Journal of Korean Astronomical Society, 48, 155

Kang, H., & Ryu, D. 2015, arXiv:1505.04256

Kocevski, D. D., Ebeling, H., Mullis, C. R., & Tully, R. B. 2007, ApJ, 662, 224

McMullin, J. P., Waters, B., Schiebel, D., Young, W., & Golap, K. 2007, Astronomical Data Analysis Software and Systems XVI, 376, 127

Noordam, J. E. 2004, in SPIE Conference Series, Vol. 5489, ed. J. M. Oschmann, Jr., 817–825s

Offringa, A. R., de Bruyn, A. G., Biehl, M., et al. 2010, MNRAS, 405, 155

Ogrean, G. A., Brüggen, M., Röttgering, H., et al. 2013, MNRAS, 429, 2617

Ogrean, G. A., Brüggen, M., van Weeren, R. J., et al. 2013, MNRAS, 433, 812

Ogrean, G. A., Brüggen, M., van Weeren, R. J., Burgmeier, A., & Simionescu, A. 2014, MNRAS, 443, 2463

Orrú, E., Murgia, M., Feretti, L., et al. 2007, A&A, 467, 943

Pacholczyk, A. G, 1970, Radio astrophysics

Paul, S., Iapichino, L., Miniati, F., Bagchi, J., & Mannheim, K. 2011, ApJ, 726, 17

Perley, R. A., & Butler, B. J. 2013, ApJS, 204, 19

Pfrommer, C., Springel, V., Ensslin, T. A., & Jubelgas, M. 2006, MNRAS, 367, 113

Russell, H. R., van Weeren, R. J., Edge, A. C., et al. 2011, MNRAS, 417, L1

Sarazin, C. L. 2002, in Astrophysics and Space Science Library, Vol. 272, 1–38

Stroe, A., van Weeren, R. J., Intema, H. T., et al. 2013, A&A, 555, A110

Stroe, A., Rumsey, C., Harwood, J. J., et al. 2014, MNRAS, 441, L41

Stroe, A., Harwood, J. J., Hardcastle, M. J., Röttgering, H. J. A. 2014, MNRAS, 445, 1213

Sunyaev, R. A., & Zeldovich, Y. B. 1972, Comments on Astrophysics and Space Physics, 4, 173

Trasatti, M., Akamatsu, H., Lovisari, L., et al. 2015, A&A, 575, A45

van Weeren, R. J., Röttgering, H. J. A., Brüggen, M., & Hoeft, M. 2010, Science, 330, 347

van Weeren, R. J., Röttgering, H. J. A., Intema, H. T., et al. 2012, A&A, 546, A124

Vazza, F., Eckert, D., Brüggen, M., & Huber, B. 2015, arXiv:1505.02782